2023

Design Rules for Sequestration of Viruses into Polypeptide Complex Coacervates

Pratik U. Joshi
Michigan Technological University

Claire Decker
Michigan Technological University

Xianci Zeng
University of Massachusetts Amherst

Arvind Sathyavageeswaran
University of Massachusetts Amherst

Sarah L. Perry
University of Massachusetts Amherst

See next page for additional authors

Recommended Citation

Joshi, Pratik U.; Decker, Claire; Zeng, Xianci; Sathyavageeswaran, Arvind; Perry, Sarah L.; and Heidt, Caryn L., "Design Rules for Sequestration of Viruses into Polypeptide Complex Coacervates" (2023). *Biomacromolecules*. 927.
https://doi.org/10.1021/acs.biomac.3c00938

Design Rules for the Sequestration of Viruses into Polypeptide Complex Coacervates

Pratik U. Joshi[1,2], Claire Decker[1], Xianci Zeng[3], Arvind Sathyavageeswaran[3], Sarah L. Perry[3,4]*, Caryn L. Heldt[1,2,*]

[1]Department of Chemical Engineering, Michigan Technological University, Houghton, MI 49931, USA

[2]Health Research Institute, Michigan Technological University, Houghton, MI 49931, USA

[3]Department of Chemical Engineering, University of Massachusetts Amherst, Amherst, MA 01003, USA

[4]Institute for Applied Life Sciences, University of Massachusetts Amherst, Amherst, MA 01003, USA

*Correspondence: heldt@mtu.edu, perrys@engin.umass.edu

Abstract

Encapsulation is a strategy that has been used to facilitate the delivery and increase the stability of proteins and viruses. Here, we investigate the encapsulation of viruses via complex coacervation, which is a liquid-liquid phase separation resulting from the complexation of oppositely charged polymers. In particular, we utilized polypeptide-based coacervates and explored the effects of peptide chemistry, chain length, charge patterning, and hydrophobicity to better understand the effects of the coacervating polypeptides on virus incorporation. Our study utilized two non-enveloped viruses, porcine parvovirus (PPV) and human rhinovirus 14 (HRV). PPV has a higher charge density than HRV, and they both appear to be relatively hydrophobic. These viruses were compared to characterize how the charge, hydrophobicity, and patterning of chemistry on the surface of the virus capsid affects encapsulation. Consistent with the electrostatic nature of complex coacervation, our results suggest that electrostatic effects associated with the net charge of both virus and polypeptide dominated the potential for incorporating virus into a coacervate, with clustering of charges also playing a significant role. Additionally, the hydrophobicity of a virus appears to determine the degree to which increasing the hydrophobicity of the coacervating peptides can enhance virus uptake. Non-intuitive trends in uptake were observed with regards to both charge patterning and polypeptide chain length, with these parameters having a significant effect on the range of coacervate compositions over which virus incorporation was observed. These results provide insight into biophysical mechanisms where sequence effects can control the uptake of proteins or viruses into biological condensates and provide insight for use in formulation strategies.

Graphical Abstract

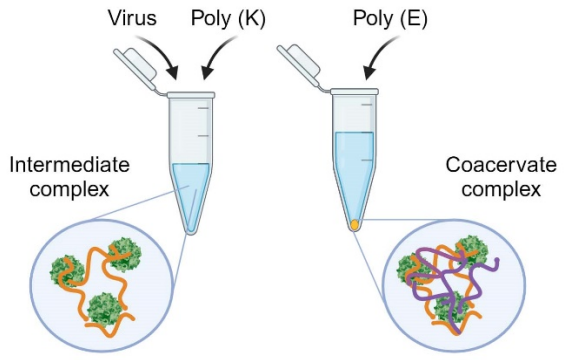

1. Introduction

Biomacromolecules, including antibodies, proteins, viruses, and RNA have seen a large growth in preclinical and clinical trials for various therapies.[1] Although these molecules have great therapeutic relevance, their ability to be delivered and remain stable both on the shelf and in the body remains a challenge. One solution to this problem is to encapsulate the biomolecule. While polymeric strategies have been increasingly used to encapsulate therapeutic proteins for delivery, the majority of polymeric approaches require the use of organic solvents, which then have the potential to denature and/or aggregate the protein cargoes.[2] In contrast, complex coacervation is a fully aqueous encapsulation strategy that has been shown to enable the controlled release of a wide range of drugs[3-8] and to improve the stability and/or shelf life of encapsulated biomacromolecules.[9-11]

Complex coacervation is an associative liquid-liquid phase separation phenomenon that can occur between mixtures of oppositely-charged macro-ions such as polyelectrolytes, proteins, surfactant micelles, and nanoparticles.[5,12-18] This phase separation results in the formation of a dense, macro-ion-rich phase, called the coacervate phase, and a macro-ion-deficient phase, called the supernatant. The driving force for coacervation comes from a combination of the electrostatic attraction between two oppositely-charged macro-ions, and the resulting entropic gains associated with the release of bound counterions and restructuring of water upon complex formation.[15,19-24] Thus, coacervation can be affected by parameters such as the charge stoichiometry of the system,[25-27] the ionic strength,[14,16,28-31] solution pH,[26,28,32,33] the size and/or net charge of the macro-ions,[29,30,34-38] as well as charge density and/or distribution of charges.[14,21,22,39-47]

While many of the reports leveraging complex coacervation for the encapsulation of proteins or other biomacromolecules might frame the discussion in terms of 'encapsulating cargo,' it would be inaccurate to think of such molecules as being simple, non-interacting guest molecules. For proteins in particular, both the net charge and the distribution of charges on the protein surface are important factors in driving incorporation.[47-51] While theoretical approaches for describing complex coacervation involving oppositely-charged polymers have begun to mature,[19,25,44,52-58] formalized frameworks for understanding complex coacervation involving globular proteins are still lacking. Such protein-containing systems are complicated by the complex surface display of different chemistries, including patches of charge, as well as the 3D geometry of the biomacromolecule. The complexity of these interactions increases the potential for fine-tuning interactions with the protein surface but makes it difficult to predict how a biomacromolecule might partition into a coacervate.

Previously, we investigated the incorporation of the model globular proteins albumin, hemoglobin, and lysozyme into complex coacervates formed from oppositely-charged polypeptides (*e.g.*,

poly(lysine) and poly(glutamate)), with a goal of establishing design rules for this 'encapsulation.'[51] The results of that study highlighted the importance of electrostatic effects, with the net charge of the protein and the distribution of charges on the surface controlling the partitioning of protein into the coacervate. For example, while maximum coacervate formation for coacervates formed in the absence protein occurred with a net neutral mixture of polypeptides (*i.e.*, equal numbers of oppositely-charged polymers), the highest levels of albumin incorporation (a protein with a net-negative charge) were observed at conditions where an excess of polycation was present. Solution conditions related to electrostatics such as pH and ionic strength also affected the incorporation in a way that was consistent with simple electrostatic intuition, as did the charge density of the polypeptides. Interestingly, though, consistent trends were not identified with regards to the polypeptide chain length.

Having established the importance of net charge and charge density on the incorporation of globular proteins, we next sought to test the interaction of viruses with polypeptide-based complex coacervates. This extension of our initial work was particularly interesting because although virus capsids are self-assembled from repeating protein subunits, viruses are structurally unique compared to smaller proteins. In particular, the larger size, charge density, and hydrophobicity of non-enveloped viruses is known to change their behavior in solution as compared to smaller proteins,[59] and enveloped viruses include the additional complication of an encapsulating lipid bilayer. Thus, we sought to determine whether the same coacervation strategies used for smaller proteins would work to incorporate viruses. Our initial study considered encapsulation of the non-enveloped porcine parvovirus (PPV) and the enveloped bovine viral diarrhea virus (BVDV).[9] Both viruses partitioned strongly into the dense coacervate phase over a range of polypeptide compositions that was consistent with the anticipated net charge of the capsids based on the acidic values of their isoelectric points (IEP),[60] similar to what had been observed for albumin in our initial study. Thus, at least for these two model systems, incorporation into complex coacervates appears to be dominated by net charge in a way that is similar to smaller globular proteins.

Here, we seek to expand our understanding of non-enveloped virus incorporation into polypeptide-based complex coacervates by varying aspects of both the polypeptides and the identity of the virus. In particular, we explore how changing the chemistry, length, charge density, charge patterning, and hydrophobicity of the polypeptides affects the encapsulation of both porcine parvovirus (PPV) and human rhinovirus (HRV) in complex coacervates.

2. Materials and Methods

The zwitterionic buffer (4-(2-hydroxyethyl)-1-piperazineethanesulfonic acid) (HEPES, ≥99%), N,N-dimethylformamide (DMF), dichloromethane (DCM), anhydrous ethyl ether, acetonitrile,

hydrochloric acid (HCl), and sodium hydroxide (NaOH) were purchased from Fisher Scientific. Piperidine, ethyl(hydroxyiminio)cyanoacetate (Oxyma), and trifluoroacetic acid (TFA), Fmoc-*L*-Lys(Boc)-OH, Fmoc-*D*-Lys(Boc)-OH, Fmoc-*L*-Glu(OtBu)-OH, Fmoc-*D*-Glu(OtBu)-OH, Fmoc-*L*-Leu-OH, and α-cyano-4-hydroxycinnamic acid were purchased from Sigma Aldrich, St. Louis, MO. Fmoc-Gly-OH and Fmoc-*L*-Ala-OH were purchased from Protein Technologies Inc., Tucson, AZ. Rink amide MBHA resin with a loading capacity of 0.643 mmol/g was purchased from P3 Biosystems, Louisville, KY. N,N-diisopropylcarbodiimide (DIC, 99%) was purchased from Acros Organics, Waltham, MA. Triisopropylsilane (TIPS) was purchased from Chem-Impex International, Wood Dale, IL. All chemicals were used as-received, without further purification.

Poly(*L*-lysine trifluoroacetate) and racemic poly(*D,L*-glutamate sodium salt) with chain lengths of 400, and 800 (K_{400}, K_{800}, E_{400}, E_{800}), as well as poly(*L*-arginine hydrochloride) with a chain length of 50 (R_{50}), were purchased from Alamanda Polymers, Huntsville, AL, and used without further purification. Shorter polymers of poly(*L*-lysine trifluoroacetate) and poly(*D,L*-glutamate sodium salt) with a degree of polymerization of N = 48 (K_{48}, E_{48}) and copolymers of lysine or glutamate with glycine, alanine, and leucine were made in-house via solid-phase synthesis. A summary of these polymers is given in Table 1.

Table 1. Table of counter-ions, molecular weights and polydispersity index (PDI) of polypeptides.

Name	Counter Ion	M_w (g/mol)	M_n (g/mol)	N	PDI[e]
K_{48}	TFA^-	-	6,334[a]	48[a]	-
E_{48}	Na^+	-	6,236[a]	48[a]	-
R_{50}	Cl^-	-	10,400[c]	54[c]	1.03
K_{400}	TFA^-	97,000	95,300[b]	394[b]	1.08
E_{400}	Na^+	60,000	59,000[c]	391[c]	1.01
K_{800}	TFA^-	194,000	183,700[c]	759[c]	1.06
E_{800}	Na^+	120,000	118,400[d]	784[d]	1.06
$(KG)_{24}$	TFA^-	-	4,485[a]	48[a]	-
$(K_2G_2)_{12}$	TFA^-	-	4,466[a]	48[a]	-
$(K_4G_4)_6$	TFA^-	-	4,448[a]	48[a]	-
$(K_8G_8)_3$	TFA^-	-	4,464[a]	48[a]	-
$(K_2A_2)_{12}$	TFA^-	-	4,799[a]	48[a]	-
$(K_2L_2)_{12}$	TFA^-	-	5,798[a]	48[a]	-
$(EG)_{24}$	Na^+	-	4,497[a]	48[a]	-
$(E_2G_2)_{12}$	Na^+	-	4,497[a]	48[a]	-
$(E_4G_4)_6$	Na^+	-	4,498[a]	48[a]	-
$(E_8G_8)_3$	Na^+	-	4,507[a]	48[a]	-

[a] Determined by MALDI-TOF. The weights of the TFA^- counterion are excluded from the reported M_n values
[b] Determined by light scattering, as reported by the manufacturer.
[c] Determined by ^1H NMR, as reported by the manufacturer.
[d] Determined by viscosity, as reported by the manufacturer.
[e] Determined by gel permeation chromatography (GPC), as reported by the manufacturer.

For cell culture, Eagle's minimum essential media (EMEM), phosphate buffered saline (PBS, pH 7.2), penicillin-streptomycin (pen-strep), trypsin containing EDTA, and fetal bovine serum (FBS, USDA approved) were purchased from Life Technologies, Carlsbad, CA. 2-(3,5-diphenyltetrazol-2-ium-2-yl)-4,5-dimethyl-1,3thiazolebromide (98%, MTT) was purchased from Alfa Aesar, Haverhill, MA, and sodium dodecyl sulfate (SDS, BioReagent, ≥98.5%) was purchased from Sigma Aldrich.

Deionized water was obtained from a Milli-Q water purification system (MilliporeSigma, Burlington, MA) or a Nanopure water system (Thermo Fisher, Waltham, MA) at a resistivity of 18.2 MΩ cm.

2.1 Peptide Synthesis and Characterization

Most of the polypeptides used in this study were prepared using standard Fmoc-based solid-phase synthesis on a Liberty Blue automated microwave peptide synthesizer from CEM Ltd., as described previously.[21] In brief, the synthesis was done using a rink amide MBHA resin at an 0.1 mmol scale. Amino acids with alternating chirality were used in the synthesis of both K_{48} and E_{48} to prevent the formation of hydrogen bonds between complexing chains.[61-63] The synthesis of copolymers of lysine or glutamate with glycine, alanine, and leucine was performed with all *L* amino acids. Fmoc deprotection was done using a solution of 20% piperidine in DMF. 0.5 M DIC and 1 M Oxyma DMF were used as activator and base, respectively. A cleavage cocktail containing TFA/water/TIPS in a volumetric ratio of 95/2.5/2.5 was used to perform side chain deprotection and cleavage of the peptide from the resin. Cold anhydrous ethyl ether (-80°C) was used to precipitate the crude polypeptide. The solution was then centrifuged (Thermo Scientifc Sorvall Legend X1R Centrifuge) for 5 min at 3500 RPM (1739×*g*) and 25°C. The ether was then decanted and the peptide was lyophilized (Labconco FreeZone 2.5 Plus).

Characterization of the final polypeptides was performed using a Bruker UltrafleXtreme matrix-assisted laser desorption/ionization time of flight mass spectrometer (MALDI-TOF). Samples of approximately 1 mg/mL peptide were mixed with different amounts of matrix. The matrix consisted of 20 mg/mL of α-cyano-4-hydroxycinnamic acid in a 1:1 volumetric mixture of water and acetonitrile with 0.01% TFA. Data collection was performed in one of two modes, depending on which gave the better signal-to-noise ratio: linear positive mode (LP 5- 50 kDa and LP 700-3500 Da) and reflector positive

mode (RP 5-50kDa and RP 700- 3500 Da). Slightly different protocols were used depending on the molecular weight of the peptide. Mass spectra are available in **Figure S1**.

2.2 Virus Propagation and Titration

PPV NADL-2 strain, donated by Dr. Ruben Carbonell (North Carolina State University, NC), was propagated in porcine kidney cells (PK-13, ATCC CRL-6489) cultured in EMEM as described previously.[64] HRV-14 strain 1059 (ATCC VR-284) was propagated in H1HeLa cells (ATCC CRL-1958) and cultured in EMEM as described previously.[65] Virus stocks were clarified to remove cell debris by spinning at 4500 rpm (3850×*g*) in a Sorvall ST16R centrifuge (Thermofisher). The clarified stocks were stored at -80°C and thawed before use, unless otherwise noted. Both viruses were titrated in their respective cell lines using a colorimetric cell proliferation MTT assay, as described previously, and reported as infectious titer in MTT_{50}/mL.[65] The MTT assay is a cell viability assay that determines the virus concentration that causes cytopathic effect in 50% of the cells.

2.3 Preparation of Stock Solutions

Stock solutions of HEPES buffer were prepared gravimetrically at a concentration of 400 mM and adjusted to a pH of 8.00 ± 0.03 using 1 M HCl and 1 M NaOH, as needed. Stock solutions for each of the polypeptides were prepared gravimetrically at a concentration of 20 mM on a total ionizable monomer basis in 10 mM HEPES and adjusted to a pH of 8.00 ± 0.03. 2 M NaCl was made with no pH adjustment.

2.4 Virus Encapsulation

Virus encapsulation into complex coacervates was achieved by mixing clarified virus stock with pH 8 HEPES stock buffer in a 1.5 mL microcentrifuge tube followed by the polycation to form an intermediate complex. After vortexing for 5 s, the polyanion was added to the mixture and vortexed for another 5 s. Samples were prepared such that the final HEPES buffer concentration was 10 mM. The charge fraction of the mixture was varied by changing the relative amounts of the polycation and polyanion while keeping the total polypeptide concentration constant at 7 mM on an ionizable monomer basis. Thus, a 1:1 ratio of polycation and polyanion would correspond to a charge fraction of 0.5 (see **Figure 1d**). These values of charge fraction do not take the virus into account.

The 240 µL coacervate systems were centrifuged at 21475×*g* at 15°C for 20 min in a ST16R centrifuge to sediment the dense coacervate phase. The supernatant was decanted into a separate tube and the coacervate phase was disassembled with 240 µL of 2 M NaCl followed by vortexing for 5 s. The samples were titrated with the MTT assay, described previously, to determine the infectious virus titer in both phases. All data was collected in triplicate and the error bars are the standard deviation of the

triplicates. The partition coefficient (P), describing the viral particles in the coacervate phase relative to the supernatant phase, was calculated as

$$P = \frac{T_C}{T_S} \quad (1)$$

where T_C and T_S are the virus titers (MTT_{50}/mL) in the coacervates and supernatant phases, respectively. The volume of the phases was not taken into account since the volume of each phase had the same post-disassembly volumes. All conditions were tested in triplicate and the standard deviation is shown as error bars.

2.5 Virus Capsid Charge and Hydrophobicity Calculations

PDB structural information from PDB ID 1K3V[66] and 4RHV[67] were used to model PPV and HRV, respectively. The proteins were prepared assigning protonation states at pH 8 using PROPKA and AMBER forcefields on the Poisson-Boltzmann server.[68,69] The electrostatic potential across the proteins were determined using the Adaptive Poisson-Boltzmann Solver (APBS) with a protein dielectric constant of 2 and solvent dielectric constant of 78.54.

Visualization of capsid structures was performed by fetching the PDB in ChimeraX 1.3 and selecting biological assemblies to construct a 3D structure.[70] The electrostatic potential maps computed with APBS were assigned to the 3D structure to generate color maps of the capsids. The color scale was normalized to yield a consistent gradient between PPV and HRV for comparison. The constructed assemblies were grayed with only the charged residues aspartate (D), glutamate (E), lysine (K), and arginine (R) colored. Possible pH effects on the charge of the N and C termini of the protein were not taken into account. Hydrophobic patchiness was identified by assigning a color gradient based on the molecular lipophilicity potential[71] to alanine (A), tryptophan (W), leucine (L), valine (V), phenylalanine (F), and isoleucine (I).

The surface accessible residues of the capsids were extracted from the CapsidMaps, an API included on the VIPERdb website.[72,73] A python code was written to extract the charged or hydrophobic residues that were identified from the CapsidMaps for the two viruses. The distance between the identified charged or hydrophobic residues was determined using the spatial coordinates from the PDB files. This information was then used to calculate a radial distribution function g(r), also known as a pair correlation function, between the charged or hydrophobic residues to identify the presence of patches on the protein surface. Briefly, the charged or hydrophobic residues were identified and then indexed. For each of the residues in turn, the number of the specified type of residues within a specified radius was

counted. This number was then normalized based on the number of total residues, the volume of the shell considered, and the particle density. The code is available in the Supplemental Information.

3. Results and Discussion

The goal of this study was to understand how variations in both the virus surface chemistry and the physicochemical characteristics of the coacervating polypeptides affect virus incorporation into complex coacervates. In particular, we investigated the encapsulation of two non-enveloped viruses, PPV and HRV (**Figure 1a**). A summary of the physical properties for PPV and HRV is given in **Table 2**. We varied the chemistry, length, charge density, charge patterning, and hydrophobicity of the polypeptides used to drive coacervation (**Figure 1b-c**) to gain a more detailed understanding of how large macromolecules encapsulate into the dense liquid phase due to the presence of charged polymers. The charge fraction is defined with respect to the fraction of positive polymers present in the system (on a monomer basis). The relationship between charge fraction and the ratio of positive to negative charges is shown in **Figure 1d**.

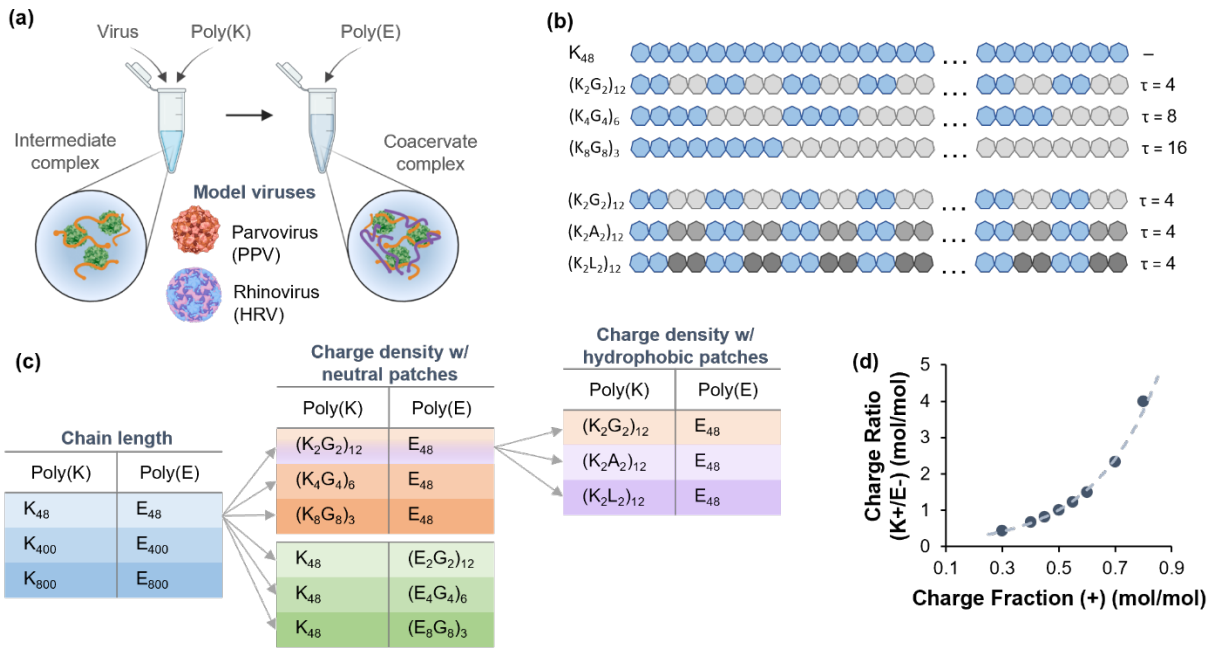

Figure 1. Coacervate design using sequence-defined block-co-polypeptides. (a) Schematic depiction of virus-containing coacervate formulation. **(b)** Example depiction of the variations in polypeptide charge density and hydrophobicity of the cationic, lysine (K)-containing polymers. Charge blockiness is defined by the parameter τ, while hydrophobicity is indicated by the color of the grey blocks as the neutral amino acid spacers go from glycine (G) to alanine (A) to leucine (L). **(c)** Experimental design matrix to study the effect of polypeptide characteristics such as charge patterning and hydrophobicity on virus encapsulation. **(d)** Plot of charge ratio (K+/E-) as a function of the total cationic charge fraction from the polypeptides present in the system. The dashed line represents a guide to the eye. Some images made with BioRender.com.

The choice of PPV and HRV allows for a comparison of size and surface chemistry. Both viruses have an IEP < 7.0, meaning that they are negatively charged at pH 8. PPV is slightly smaller than HRV and has a very regular T1 triangulation. This structure designation means that there are 60 proteins on the surface of the virus that form an icosahedron. Of these 60 proteins, 80% or more are VP2, followed by VP1 and VP3.[66] VP2 and VP3 are cleavage products of VP1. Therefore, PPV has a very regular structure that can effectively be described as involving a single protein. In contrast, HRV has three distinct proteins on its surface, VP1, VP2, and VP3. VP4 is present on the interior of the capsid and provides an anchor for the genome.[74] The structure of HRV is pseudo T3, which means that the icosahedral structure is formed from 60 units of three proteins, resulting in 180 proteins on the surface of the capsid. Additional aspects of the physicochemical properties of the two capsids will be discussed in Section 3.4 below.

Table 2. Virus capsid characteristics.

Virus	Family	Genome	T#	Size (nm)	IEP	Capsomeres	Refs.
Porcine parvovirus (PPV)	Parvoviridae	ssDNA	1	18-26	4.8-5.1	VP1, VP2, VP3	60,66
Human rhinovirus 14 (HRV)	Picornaviridae	ssRNA	p3*	30	6.9	VP1, VP2, VP3, VP4	74-76

* pseudoT3

3.1 Virus Encapsulation Varies with Polymer Chain Length

To begin with, we studied the effect of polypeptide length on virus incorporation. For each different length system (N = 48, 400, 800), we prepared coacervate samples at a constant total concentration of charged peptide, but different relative amounts of poly(lysine) and poly(glutamate) (*i.e.*, cationic charge fraction). For each of these coacervate systems we tracked the virus titer in both the supernatant and the dense phase to identify the optimum conditions for virus incorporation. Both PPV and HRV carry a net negative charge at pH 8.0. Thus, based on our previous efforts, we expected to observe strong virus incorporation at conditions where the coacervate carried a net positive charge.[9,51]

As shown in **Figure 2a-f**, starting from an initial titer of ~8 log PPV and ~7 log HRV, we observed that nearly all of the virus was present in the supernatant at low cationic charge fractions where phase separation was expected to be minimal. We then observed a decrease in the amount of virus present in the supernatant with increasing charge fraction, coupled with an increase in the amount of virus present in the coacervate. For each coacervate system, we observed an optimum condition where a maximal amount of virus was incorporated into the coacervate – to the point that the titer levels in the supernatant reached the limit of detection. Beyond this optimum, the amount of virus in the supernatant then increased again with increasing charge fraction. These trends can be examined by considering both the raw titer

data (**Figure 2a-f**), and plots of the natural log of the partition coefficient ($ln(P)$, see Eq. 1) for the virus (**Figure 2g,h**).

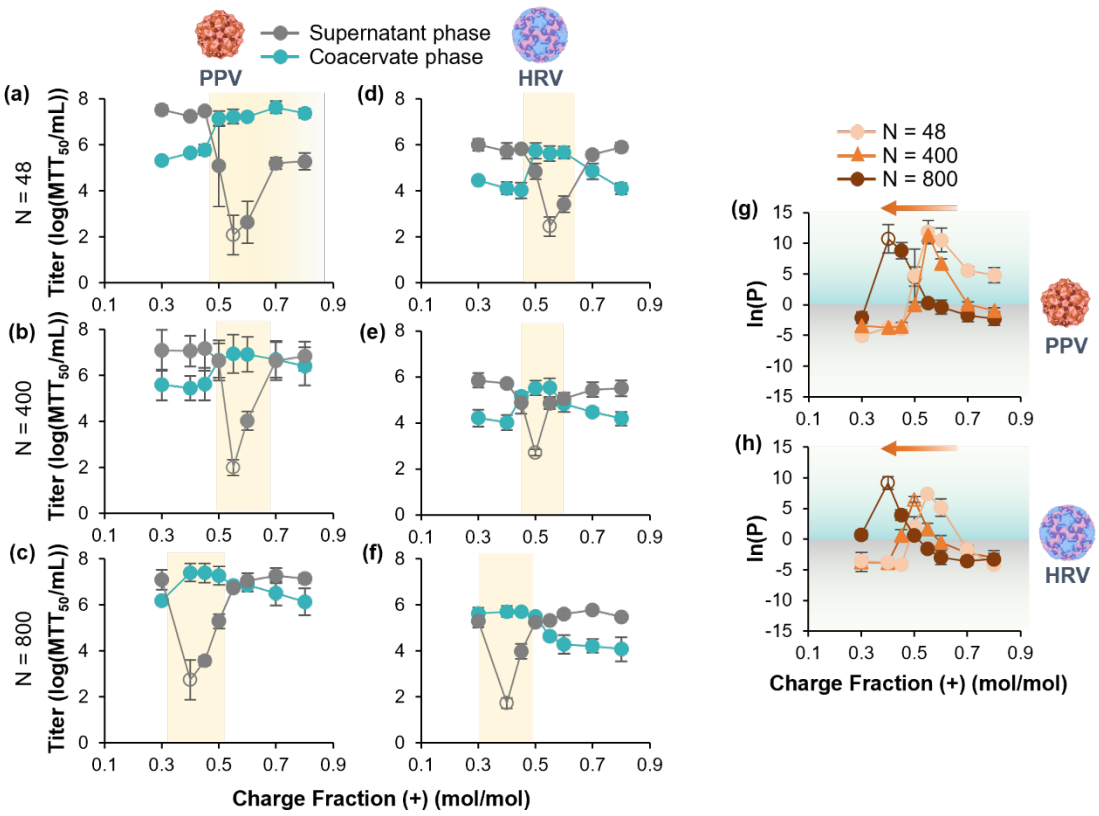

Figure 2. Trends in virus encapsulation as a function of polypeptide chain length. (a-c) PPV and **(d-f)** HRV titers in the supernatant and coacervate phases as a function of charge stoichiometry for coacervates formed from poly(lysine) and poly(glutamate) of chain length N = 48, 400, and 800. Yellow boxes highlight the range of charge fractions over which $ln(P) > 0$. **(g,h)** The corresponding partition coefficient $ln(P)$ for **(g)** PPV and **(h)** HRV as a function of charge stoichiometry showing the shift towards lower charge fraction with increasing chain length. Coloring of the background in the plots indicates when $ln(P)>0$, meaning that the virus preferred the coacervate phase and $ln(P)<0$ represents the virus preferring the supernatant phase. The data are the average of three encapsulation experiments with the error bars shown as the standard deviation of the replicate measurements. Open symbols indicate the data were measured at the limit of detection of the MTT assay.

Interestingly for the 48-mer system, we observed a high virus titer in the supernatant at low cationic charge fractions, even though the sample appeared turbid, suggesting the formation of a coacervate (**Figure S2**). Additionally, while we observed a full recovery of the initial virus titer in the supernatant and a loss of titer in the coacervate at high cationic charge fractions for HRV (**Figure 2d**), only a partial recovery was observed for PPV (**Figure 2a**), despite a lack of turbidity in the sample (**Figure S2a**). We hypothesize that the apparent high levels of virus present in the 'coacervate' phase when bulk phase separation was not observed is the result of sedimentation of nanometer-scale 'soluble complexes' that are stabilized by the presence of excess polycation. In fact, we observed similar titer

levels at cationic charge fractions of 0.7 and 0.8 when PPV was mixed with only K_{48} as when it was mixed with both K_{48} and E_{48} (**Figure S3**).

For both the 48-mer and 400-mer systems, our virus incorporation results were consistent with our expectations based on the net charge of the viruses and our previous results. For PPV, the titer in the supernatant for both of these coacervate systems reached the limit of detection at a charge fraction of 0.55 (**Figure 2a,b**), while for HRV we observed a slight shift in this optimal condition from 0.55 for the 48-mers to 0.50 for the 400-mers (**Figure 2d,e**). However, for the longest polypeptide system with N = 800, we observed a significant shift in the conditions over which virus incorporation was observed, with maximum incorporation observed to the limit of detection at a cationic charge fraction of 0.40 (**Figure 2c,f**). These same trends can be observed by considering a plot of virus partition. The range of conditions over which preferential incorporation of virus into the coacervate phase occurred, ($ln(P) > 0$), defined in Eq. 1, and colored light blue), as well as the maximum partitioning, shifted towards lower cationic charge fractions with increasing polypeptide length. (**Figure 2g,h**). Additionally, these data highlight that the range of conditions for virus incorporation was narrower for HRV than PPV (**Figure 2a-f**, shown in yellow), and that the longest polypeptide system resulted in an increase in virus partitioning for HRV, but showed no change for PPV.

It is unclear from a mechanistic perspective why the partitioning obtained for systems of longer polypeptides shifts away from conditions that are closer to net neutrality, and towards polymer mixtures that are 'net negative.' One potential factor is the relative difference in the size of the various length polymers relative to the virus capsid. If the estimated peptide contour length is 3.5Å,[77] then an 800-mer is approximately 280 nm if stretched out to full length. While we know the peptide is not fully stretched out in solution, the length-scales of our longer polypeptides are sufficient for the peptide to wrap around (a single capsid is only about 20 nm in diameter) and potentially bridge two capsids, while such bridging would not be expected for shorter polypeptides. It is possible, therefore, that the closely interacting viruses and the complexing polycations may shield some of the charge or cause an excluded volume effect where the interactions needed to achieve charge neutralization are either not possible or not energetically favorable. Reports in the literature have described similar interactions between surfactant micelles and charged polymers, where the optimum charge ratio for complexation was not 1:1.[78]

While significantly higher values of $ln(P)$ were obtained for PPV, as compared to HRV, and these differences increased with decreasing chain length, the overall trends in our data appear to be relatively independent of the identity of the virus. Thus, differences in the capsid size and the composition and/or clustering of charge or hydrophobicity on the surface of the capsid may not have a significant effect on the range of conditions over which virus uptake is observed, or the composition of the optimal

formulation, if only chain length is considered. Ultimately, it may be difficult to parse out the molecular-level mechanistic details that modulate virus incorporation without insight from computational models.

3.2 Virus Encapsulation and Polycation Identity

We also investigated the effect of changing the cationic polypeptide from polylysine (K_{48}) to polyarginine (R_{50}). We were particularly interested in arginine as a potential system. Arginine is a unique molecule that at acidic pH can inactivate enveloped viruses,[79,80] but can also be found in viral vaccine formulations.[81] Arginine has also been shown to disrupt hydrophobic interactions.[82] While preliminary data showed similar trends for the incorporation of both PPV and HRV into complexes formed with either polycation (see **Figure S4**), solid aggregates were observed instead of a dense liquid coacervate phase, as shown in **Figure S5**. Thus, we elected to not pursue additional studies with arginine-containing polypeptides.

3.3 Virus Encapsulation and Polypeptide Charge Patterning

To study the effect of charge patterning the polypeptides, we examined virus incorporation into coacervates formed from 48-mer polypeptides of lysine-*co*-glycine and glutamate-*co*-glycine. Each of the peptides is half-charged, meaning that 24 of the 48 residues are glycine. The various charged or neutral residues are arranged in regular repeating patterns that can be described by the parameter τ, which describes the number of residues in a repeat unit and scales with the blockiness of the pattern (**Figure 1b,c**). For example, a pattern of two lysines and two glycines (*i.e.*, $(K_2G_2)_{12}$) would have $\tau = 4$, while $(K_8G_8)_3$ has $\tau = 16$. Previous experiments with small, globular proteins using homopolymers and half-charged polypeptides with $\tau = 2$ indicated that the net charge of the polymer dictated protein incorporation, such that using a half-charged polypeptide that had the same charge as the protein decreased competition for binding and enhanced partitioning. Similarly, decreasing the charge density of the polypeptide with the opposite charge as the protein adversely affected binding.[51] However, these studies only considered the effect of charge density, and not the patterning of charges on the polymer chain. Thus, to focus on the effects of patterning, we only considered complex coacervates where one of the half-charged copolypeptides was paired with the oppositely-charged homopolypeptide (*i.e.*, K_{48} or E_{48}).

For PPV we observed a slight decrease in the maximum level of partitioning into the coacervate phase when going from a fully charged K_{48} system to a half-charged lysine-glycine copolymer, in complex with E_{48}. While this result was consistent with our previous experiments with small proteins, it was interesting to note that we also observed a significant shift in the range of charge fractions over which incorporation occurred. Maximum PPV partitioning into the coacervate phase shifted from a cationic

charge fraction of 0.55 for the fully-charged K_{48}/E_{48} system towards higher cationic charge fractions when copolymers of lysine and glycine were used (**Figure 3a**). We observed no significant differences between the various lysine copolymers. Additionally, for both the homopolymer system and the lysine copolymers we observed an asymmetric 'tailing' in the partitioning at high charge fractions. As was discussed above, we hypothesize that the high levels of virus incorporation at high charge fractions may be the result of the polycations interacting strongly with the capsid.

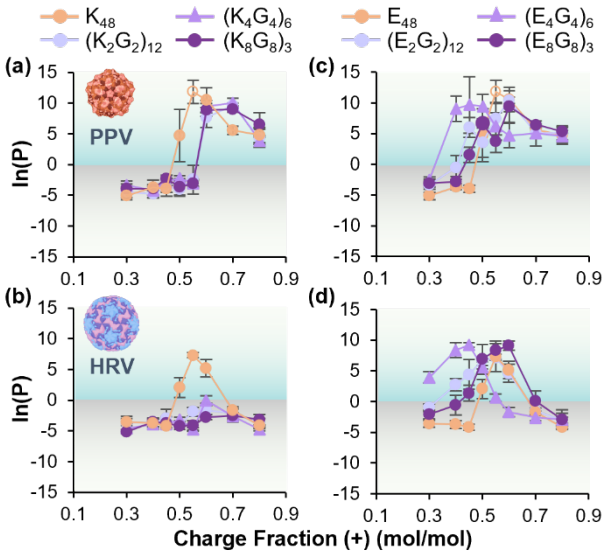

Figure 3. Trends in virus encapsulation as a function of polypeptide charge density. Plot of $ln(P)$ as a function of charge stoichiometry for **(a,c)** PPV and **(b,d)** HRV in coacervates made from charge-patterned polypeptides (N = 48) of **(a,b)** K_nG_n with E_{48} and **(c,d)** K_{48} with E_nG_n. Coloring of the background in the plots indicates when $ln(P)>0$, meaning that the virus preferred the coacervate phase and $ln(P)<0$ represents the virus preferring the supernatant phase. The data are the average of three encapsulation experiments with the error bars shown as the standard deviation of the replicate measurements. Open symbols indicate the data were measured at the limit of detection.

For the opposite case, where half-charged copolymers of glutamate and glycine were mixed with K_{48}, the trends of PPV incorporation were far less affected by sequence. Overall, changing the charge patterning of the polyglutamate did not significantly change either the maximum partitioning or the overall trend in partitioning as compared with the K_{48}/E_{48} system, with the exception of $(E_4G_4)_6$ which showed a shift to lower charge fractions (**Figure 3c**). While a mechanistic understanding of the effect of charge patterning on virus incorporation is beyond the scope of the current work, we hypothesize that the size of the charge blocks on the $(E_4G_4)_6$ peptide might represent a balancing of electrostatic repulsion and attraction between the PPV capsid and the K_{48} peptide such that incorporation can occur at lower charge fractions.

In contrast to the results from PPV, significant incorporation of HRV was only observed for the fully-charged K_{48}/E_{48} system. Coacervates involving lysine/glycine copolymers did not preferentially incorporate HRV as compared to the supernatant, regardless of charge block size (**Figure 3b**). However, similar trends in partitioning were observed for HRV as compared to PPV for the glutamate/glycine copolymers (**Figure 3d**). The titer data for PPV and HRV in both the coacervate and supernatant can be found in **Figures S6** and **S7**.

The differences and similarities in the partitioning trends between the various patterned polycations and polyanions and the two virus systems are interesting in that they hint at the impact of both polypeptide and virus properties. As might be expected for a negatively-charged biomacromolecule, our data indicate that the overall trends in the partitioning are dominated by the polycation characteristics. A closer analysis of the distribution of charges on the virus capsids is needed to further parse our results.

3.4 Charge and Electrostatic Potential Distribution on Virus Capsid

We selected the two virus for this study due to their structural differences. While both the viruses are negatively charged at pH 8, the absolute charge of the two capsids is significantly different. For example, considering only lysine and arginine as cationic residues and aspartate and glutamate as anionic residues, HRV has more ionizable residues overall, but PPV has a significantly higher ratio of negative to positive surface residues than HRV. This difference results in a net charge of -4 per subunit vs. -2 for HRV, or -240 per PPV capsid vs. -120 for an HRV capsid (**Table 3**). These trends with regards to the number and density of ionizable residues can be visualized directly on the capsid (**Figure 4a,b**), and the dramatic differences in net charge can be clearly observed when a structural depiction of the two capsids is colored based on electrostatic potential (**Figure 4c,d**).

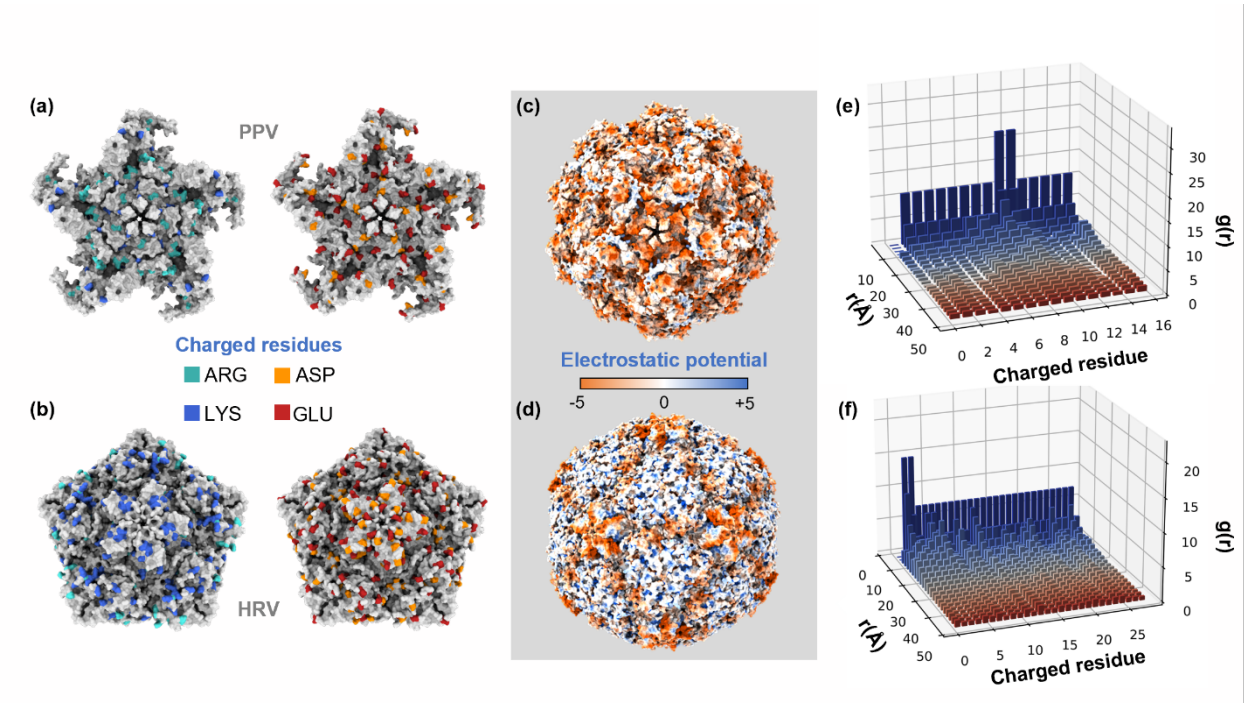

Figure 4. Virus surface charge. Structural depiction of the location of **(a,b)** charged residues and **(c,d)** the resulting electrostatic potential on the **(a,c)** PPV (PDB: 1K3V[66]) and **(b,d)** HRV (PDB: 4RHV[67]) capsid. The protonation state was calculated at pH 8 using PROPKA method on Poisson-Boltzmann server considering lysine (K), arginine (R), glutamate (E), and aspartate (D) as the ionizable residues. Images were generated using ChimeraX 1.3. Radial distribution function (g(r)) with respect to each charged residue on the **(e)** PPV and **(f)** HRV subunits. Only the charged residues that appear on the capsid surface and are solvent accessible were considered in this calculation.

Table 3. Charge and hydrophobicity of solvent accessible surface residues for PPV and HRV capsids, as extracted from CapsidMaps.[72,73]

	Per Subunit		Per Capsid	
Features	**PPV**	**HRV**	**PPV**	**HRV**
Total negative residues (N)	10	15	600	900
Total positive residues (P)	6	13	360	780
charge ratio (N/P)	1.7	1.2	1.7	1.2
Charge fraction (N/(N+P))	0.625	0.536	0.625	0.536
Total charge	-4	-2	-240	-120
Total hydrophobicity	7.1	10.4	428.4	623.4

Interestingly, the net charge differences on the capsids did not significantly affect the charge fraction at which maximum partitioning was observed for the homopolypeptide system, regardless of chain length (**Figure 2**). However, it is possible that the higher net charge of PPV was responsible for the wider range of charge fractions over which incorporation was observed, potentially due to strong

interactions between the capsid and the positively-charged polypeptide. We also speculate that the higher net charge of PPV facilitated uptake into coacervates composed of less strongly interacting lysine/glycine copolymers, whereas preferential partitioning did not occur for HRV (**Figure 3a,b**).

In addition to the absolute value of the charge, the distribution of charges on the surface of the PPV and HRV capsids can play an important role in driving incorporation. Examination of the electrostatic surface potential on the capsids in **Figure 4c,d** clearly highlights the significant differences in charge clustering between PPV and HRV. Overall, PPV appears to have a comparatively uniform charge distribution on the capsid, as compared to HRV. This is likely due to PPV only having one main capsid protein. Both viruses have a concentration near the five-fold axis of negative electrostatic potential, the HRV capsid has a relatively higher positive potential between the adjacent pentamers than PPV (**Figure 4c,d**). This may be due to there being different proteins in HRV that make up the capsid. A more detailed analysis of the various proteins that contribute to the HRV capsid demonstrated that most of the capsid charge comes from VP1 (**Figure S8**).

To translate these qualitative observations regarding charge clustering into a more quantitative metric, we performed a radial distribution analysis for each of the ionizable residues on the capsid surface. The more uniform charge distribution can also be seen in the radial distribution function ($g(r)$) shown in **Figure 4e,f.** For PPV, $g(r)$ is fairly uniform, with one spike that likely corresponds to the five-fold axis. For HRV, there is one spike in the *g(r)* that represents the five-fold axis. The rest of the surface exposed charged amino acids are very far from other charged residues, as shown by the low value of *g(r)* for the rest of the capsid. The $g(r)$ plots shown in Figure 4 are only for the charged residues that can be found on the surface of the virus. These same calculations were done for the entire virus capsid protein and can be seen in **Figure S9**. A very different story emerges if the entire capsid protein is taken into account. However, this is not an accurate method to determine surface charge interactions.[59,83] Only surface exposed amino acids should be used to determine surface interactions.

The charge clustering on the virus explains some of the results for encapsulation as the charge density of the peptides was reduced. For the K_{48}/E_{48} system, a maximum value of $ln(P) = 7.3$ was obtained for HRV, while a value of $ln(P) = 11.8$ was determined for PPV. Similarly, the lower degree of charge clustering likely negatively impacted the ability of HRV to interact with coacervates composed of the less-strongly interacting lysine/glycine copolymers. These results are consistent with our experiences with smaller proteins,[51] and with other reports investigating the effects of net protein charge and charge patchiness.[47-50]

3.5 Virus Encapsulation Varies with Polypeptide Hydrophobicity

Finally, we looked to examine the effect of the hydrophobicity of the neutral component of our copolypeptides. To this end, we elected to consider only copolymers of lysine in complex with a fully-charged E_{48}, as changes to the polycation had been observed to have the most dramatic impact on virus incorporation. Additionally, we only considered a single pattern, $((K_2X_2)_{12}$, see **Figure 3b,c**) in order to avoid hydrophobically-driven aggregation of peptides with larger hydrophobic blocks. In particular, we examined copolymers with increasing hydrophobicity, going from glycine < alanine < leucine. These amino acids were selected to span the more hydrophilic half of the Eisenberg hydrophobicity scale (**Figure 5a**),[84] thus reducing the chance that solubility would become an issue.

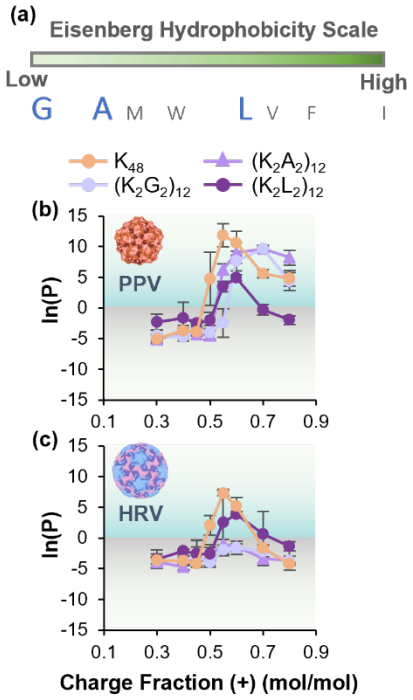

Figure 5. Trends in virus encapsulation as a function of polypeptide hydrophobicity. (a) Visual depiction of the Eisenberg hydrophobicity scale and the hydrophobic amino acids used. Plot of $ln(P)$ as a function of charge stoichiometry for **(b)** PPV and **(c)** HRV in coacervates made from charge-patterned polypeptides (N = 48) with increasing hydrophobicity (G < A < L). Coloring of the background in the plots indicates when $ln(P)>0$, meaning that the virus preferred the coacervate phase and $ln(P)<0$ represents the virus preferring the supernatant phase. The data are the average of three encapsulation experiments with the error bars shown as the standard deviation of the replicate measurements.

As was discussed above, the use of $(K_2G_2)_{12}$, the least hydrophobic residue, resulted in a slight decrease in the maximum partitioning and shifted the PPV conditions for maximum incorporation to higher charge fractions than were needed for the K_{48} homopolymer (**Figure 5b**). Additionally, a more significant 'tailing' effect was observed, with high levels of virus observed in the coacervate phase even

at the highest charge fractions tested. Changing from glycine to alanine to leucine, we observed a slight shift in the partitioning data to lower charge fractions (**Figure 5b**). Furthermore, although the initial increase in partitioning was very similar for the various peptides, we observed a peak at a charge fraction of 0.60 for the most hydrophobic, leucine-containing polypeptide, as well as less of a 'tailing' effect, and lower partitioning overall. The titers for the alanine and leucine peptide systems can be found in **Figure S10**.

In contrast to the results for PPV, the opposite trend was found for HRV. As discussed previously, HRV did not partition preferentially into coacervates formed from $(K_2G_2)_{12}$. Increasing the hydrophobicity of the polypeptide from glycine to alanine did not significantly alter this partitioning result. However, further increasing the hydrophobicity via the use of leucine resulted in significant incorporation of HRV into the coacervate phase (**Figure 5c**). The maximum incorporation of HRV was achieved at a cationic charge fraction of 0.60, higher than the peak observed for the homopolymer system.

The different trends in the data for PPV and HRV as a function of polypeptide hydrophobicity again raise the question about the role of virus surface chemistry. For these experiments, as the charge patterning of the polypeptides was kept constant, we do not anticipate that electrostatic effects should play a dominant role. Instead, we explored the distribution of neutral, nonpolar residues on the surface of the capsids. Overall, HRV is more hydrophobic than PPV (**Table 3**), and qualitative examination of the virus structure suggests the presence of hydrophobic and hydrophilic patches on both PPV and HRV (**Figure 6a,b**). While the hydrophobic amino acids might qualitatively appear to be similarly distributed on the surface of the viruses (**Figure 6c,d**), a more quantitative radial distribution analysis showed that the hydrophobic patchiness was significantly higher for HRV (**Figure 6f**) than for PPV (**Figure 6e**) for the surface exposed residues. As shown in **Figure S11**, the patchiness of the virus is less evident when the entire amino acid sequence is used in the radial distribution analysis, again demonstrating that using the entire amino acid sequence gives less insightful results than only using the surface exposed amino acids.

Taking this physicochemical picture of the number and distribution of hydrophobic residues on the surfaces of the two viruses into account, we hypothesize that the overall magnitude of hydrophobicity of the capsid surface may be the factor that explains the different trends in virus uptake. This explanation is in contrast to the results for charge, where both net charge and patchiness are important. In the context of electrostatics, the distribution of charges becomes important because charge patches are able to localize counterions, which are then released upon binding of the polymer, providing an entropic driving force for complexation. While a similar phenomenon might be expected for surface-bound water on hydrophobic patches, it is possible that the magnitude of such hydrophobic patchiness might become more relevant if polymers with longer regions of hydrophobic residues were used. Such experiments would require careful

balancing of hydrophobic polymer segments to avoid self-association and are beyond the scope of the current work. However, our observations here suggest potentially interesting trends that might be relevant to both formulation efforts using complex coacervation, and associations between proteins and/or viruses and biomolecular condensates in natural systems.[85-92]

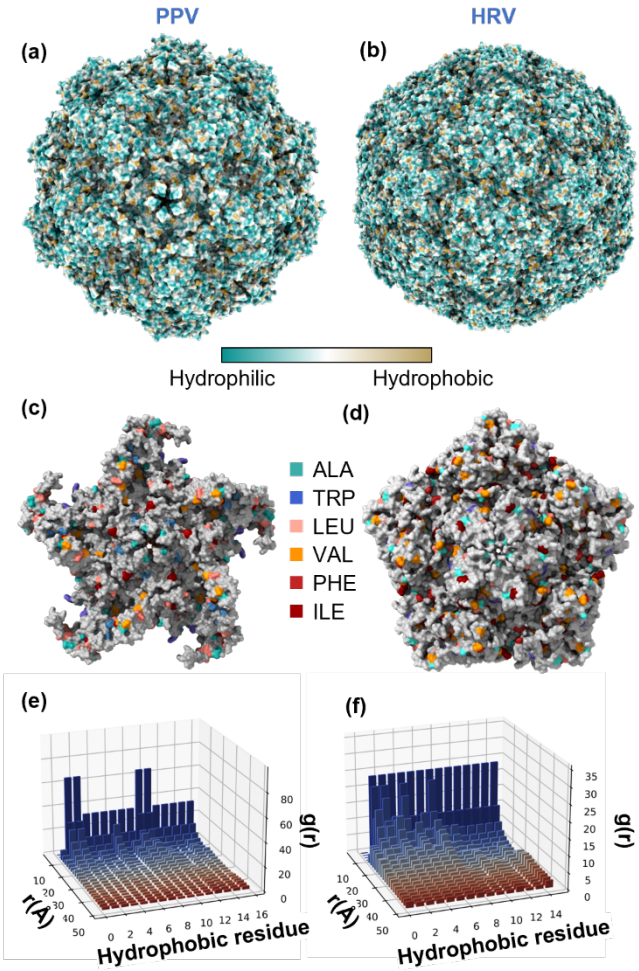

Figure 6. Virus surface hydrophobicity. Structural depiction of the location of hydrophobic residues on the **(a)** PPV (PDB: 1K3V[66]) and **(b)** HRV (PDB: 4RHV[67]) capsid. Images were generated using ChimeraX 1.3. Radial distribution function (g(r)) with respect to each hydrophobic residue on the **(e)** PPV and **(f)** HRV subunits. Only the residues that appear on the capsid surface and are solvent accessible were considered in this calculation.

4. Conclusions

In summary, we have explored how the physicochemical parameters of the charged polypeptides used to drive complex coacervation can affect the uptake of different non-enveloped viruses into the coacervate phase. In particular, we examined how variations in polypeptide chemistry, chain length, charge density, charge patterning, and hydrophobicity affect virus incorporation. Additionally, as the

virus capsids cannot be considered as merely passive guest molecules, we also correlated differences in the charge, hydrophobicity, and patterning of surface chemistry on the capsid surface with trends in partitioning.

We observed that the electrostatic effects associated with the net charge of both virus and polypeptide dominated the potential for incorporating virus into a coacervate, with clustering of charges also playing a significant role. For example, both viruses used in this study carry a net negative charge. We observed a decrease in virus incorporation when the charge density of the cationic polypeptide was decreased, meaning that the interaction between the virus and the peptides was weakened. Similarly, the lower overall net charge and charge density of HRV as compared with PPV may explain why no partitioning of HRV was observed in coacervates with a lower charge density polycation. Additionally, our results suggest that the overall hydrophobicity of a virus determines the degree to which increasing the hydrophobicity of the coacervating peptides can enhance virus uptake. However, intriguing mechanistic questions remain about how 'hydrophobic' effects might contribute to virus uptake, such as whether clustering of hydrophobic residues might lead to an enhanced energetic driving force from the restructuring of water molecules upon complex formation. Overall, the trends we observed related to electrostatics are in agreement with previous results obtained for smaller globular proteins [51]. It is unknown how hydrophobic factors might correlate between these different size biomacromolecules as data on the effect of polypeptide hydrophobicity on protein incorporation have not been reported.

Interestingly, we also observed non-intuitive trends in uptake with regards to both charge patterning and polypeptide chain length that would likely require focused mechanistic and potentially computational study to fully understand. In particular, we observed a shift in the optimal coacervate composition to lower, 'net negative' charge fractions with increasing polypeptide chain length. Additionally, we observed an increase in partitioning for the longest polypeptide chains for the larger virus HRV, but not for PPV. However, differences in the net charge and charge patchiness of the two viruses make it difficult to parse size vs. surface chemistry effects.

Overall, the results of this study expand our understanding of 'design rules' whereby biomacromolecules such as proteins and viruses can be incorporated into complex coacervates. We have previously reported on the ability for complex coacervates to explore the potential of complex coacervation to improve the thermal stability of PPV,[9] and our results here highlight the potential to extract virus from solution to the limit of detection and concentrate it in a small volume of coacervate. Future efforts will look to understand whether the interactions and effects that drive trends in encapsulation play a similar role in modulating the thermal stability of our virus formulations. This potential to extract, concentrate, purify,[49,93-96] and stabilize[9] viruses and other biomacromolecules[97-99]

could allow for the use of coacervation to enable a new generation of more stable and higher performing biologics, sensors, or biocatalysts.

Acknowledgements

The authors acknowledge the support of the National Institute of Allergy and Infectious Disease of the National Institutes of Health under award R21AI150962. The content is solely the responsibility of the authors and does not necessarily represent the official views of the National Institutes of Health. The cells to propagate the HRV were derived from a HeLa cell line. Henrietta Lacks, and the HeLa cell line that was established from her tumor cells without her knowledge or consent in 1951, have made significant contributions to scientific progress and advances in human health. We are grateful to Henrietta Lacks, now deceased, and to her surviving family members for their contributions to biomedical research.

Supplementary documents

The supplemental information contains MALDI peptide spectra, coacervate turbidity map, PPV partitioning with poly(K) only, virus partitioning with arginine, titer data for partitioning data shown in the paper, the electrostatic potential of HRV, and the radial distribution function for all residues.

A second supplemental file contains the Python codes used in this work.

References

1 Kinch, M. S., Kraft, Z. & Schwartz, T. 2021 in review: FDA approvals of new medicines. *Drug Discov Today* **27**, 2057-2064 (2022). https://doi.org:10.1016/j.drudis.2022.04.010

2 Pisal, D. S., Kosloski, M. P. & Balu-Iyer, S. V. Delivery of therapeutic proteins. *J. Pharm. Sci.* **99**, 2557-2575 (2010). https://doi.org:10.1002/jps.22054

3 Chu, H., Gao, J., Chen, C. W., Huard, J. & Wang, Y. Injectable fibroblast growth factor-2 coacervate for persistent angiogenesis. *Proc Natl Acad Sci U S A* **108**, 13444-13449 (2011). https://doi.org:10.1073/pnas.1110121108

4 Vehlow, D. *et al.* Polyelectrolyte Complex Based Interfacial Drug Delivery System with Controlled Loading and Improved Release Performance for Bone Therapeutics. *Nanomaterials (Basel)* **6**, 53 (2016). https://doi.org:10.3390/nano6030053

5 Johnson, N. R. & Wang, Y. Coacervate delivery systems for proteins and small molecule drugs. *Expert Opin Drug Deliv* **11**, 1829-1832 (2014). https://doi.org:10.1517/17425247.2014.941355

6 Chu, H., Johnson, N. R., Mason, N. S. & Wang, Y. A [polycation:heparin] complex releases growth factors with enhanced bioactivity. *J Control Release* **150**, 157-163 (2011). https://doi.org:10.1016/j.jconrel.2010.11.025

7 Johnson, N. R. & Wang, Y. Controlled delivery of heparin-binding EGF-like growth factor yields fast and comprehensive wound healing. *J Control Release* **166**, 124-129 (2013). https://doi.org:10.1016/j.jconrel.2012.11.004

8 Porcel, C. H. & Schlenoff, J. B. Compact polyelectrolyte complexes: "saloplastic" candidates for biomaterials. *Biomacromolecules* **10**, 2968-2975 (2009). https://doi.org:10.1021/bm900373c

9 Mi, X. *et al.* Thermostabilization of viruses via complex coacervation. *Biomater Sci* **8**, 7082-7092 (2020). https://doi.org:10.1039/d0bm01433h

10 Blocher McTigue, W. C. & Perry, S. L. Protein Encapsulation Using Complex Coacervates: What Nature Has to Teach Us. *Small* **16**, e1907671 (2020). https://doi.org:10.1002/smll.201907671

11 Muronetz, V. I., Pozdyshev, D. V. & Semenyuk, P. I. Polyelectrolytes for Enzyme Immobilization and the Regulation of Their Properties. *Polymers (Basel)* **14**, 4204 (2022). https://doi.org:10.3390/polym14194204

12 Nairm, J. G. in *Advances in pharmaceutical sciences* Vol. 7 93-219 (Elsevier, 1995).

13 Timilsena, Y. P., Akanbi, T. O., Khalid, N., Adhikari, B. & Barrow, C. J. Complex coacervation: Principles, mechanisms and applications in microencapsulation. *Int. J. Biol. Macromol.* **121**, 1276-1286 (2019). https://doi.org:10.1016/j.ijbiomac.2018.10.144

14 Sing, C. E. & Perry, S. L. Recent progress in the science of complex coacervation. *Soft Matter* **16**, 2885-2914 (2020). https://doi.org:10.1039/d0sm00001a

15 Srivastava, S. & Tirrell, M. V. in *Adv. Chem. Phys.* Vol. 161 *Advances in Chemical Physics* 499-544 (Wiley, 2016).

16 Marciel, A. B., Chung, E. J., Brettmann, B. K. & Leon, L. Bulk and nanoscale polypeptide based polyelectrolyte complexes. *Adv. Colloid Interface Sci.* **239**, 187-198 (2017). https://doi.org:10.1016/j.cis.2016.06.012

17 Voets, I. K., de Keizer, A. & Cohen Stuart, M. A. Complex coacervate core micelles. *Adv. Colloid Interface Sci.* **147-148**, 300-318 (2009). https://doi.org:10.1016/j.cis.2008.09.012

18 Zhao, W. & Wang, Y. Coacervation with surfactants: From single-chain surfactants to gemini surfactants. *Adv. Colloid Interface Sci.* **239**, 199-212 (2017). https://doi.org:10.1016/j.cis.2016.04.005

19 Sing, C. E. Development of the modern theory of polymeric complex coacervation. *Adv. Colloid Interface Sci.* **239**, 2-16 (2017). https://doi.org:10.1016/j.cis.2016.04.004

20 Chen, S. & Wang, Z. G. Driving force and pathway in polyelectrolyte complex coacervation. *Proc Natl Acad Sci U S A* **119**, e2209975119 (2022). https://doi.org:10.1073/pnas.2209975119

21 Chang, L. W. *et al.* Sequence and entropy-based control of complex coacervates. *Nat Commun* **8**, 1273 (2017). https://doi.org:10.1038/s41467-017-01249-1

22 Lytle, T. K., Chang, L. W., Markiewicz, N., Perry, S. L. & Sing, C. E. Designing Electrostatic Interactions via Polyelectrolyte Monomer Sequence. *ACS Cent Sci* **5**, 709-718 (2019). https://doi.org:10.1021/acscentsci.9b00087

23 Priftis, D., Laugel, N. & Tirrell, M. Thermodynamic characterization of polypeptide complex coacervation. *Langmuir* **28**, 15947-15957 (2012). https://doi.org:10.1021/la302729r

24 Fu, J. & Schlenoff, J. B. Driving Forces for Oppositely Charged Polyion Association in Aqueous Solutions: Enthalpic, Entropic, but Not Electrostatic. *J. Am. Chem. Soc.* **138**, 980-990 (2016). https://doi.org:10.1021/jacs.5b11878

25 Friedowitz, S. *et al.* Looping-in complexation and ion partitioning in nonstoichiometric polyelectrolyte mixtures. *Sci Adv* **7**, eabg8654 (2021). https://doi.org:10.1126/sciadv.abg8654

26 Knoerdel, A. R., Blocher McTigue, W. C. & Sing, C. E. Transfer Matrix Model of pH Effects in Polymeric Complex Coacervation. *J. Phys. Chem. B* **125**, 8965-8980 (2021). https://doi.org:10.1021/acs.jpcb.1c03065

27 Zhang, P., Alsaifi, N. M., Wu, J. & Wang, Z. G. Polyelectrolyte complex coacervation: Effects of concentration asymmetry. *J. Chem. Phys.* **149**, 163303 (2018). https://doi.org:10.1063/1.5028524

28 Perry, S., Li, Y., Priftis, D., Leon, L. & Tirrell, M. The Effect of Salt on the Complex Coacervation of Vinyl Polyelectrolytes. *Polymers* **6**, 1756-1772 (2014). https://doi.org:10.3390/polym6061756

29 Priftis, D. & Tirrell, M. Phase behaviour and complex coacervation of aqueous polypeptide solutions. *Soft Matter* **8**, 9396-9405 (2012). https://doi.org:10.1039/c2sm25604e

30 Li, L. *et al.* Phase Behavior and Salt Partitioning in Polyelectrolyte Complex Coacervates. *Macromolecules* **51**, 2988-2995 (2018). https://doi.org:10.1021/acs.macromol.8b00238

31 Yang, M., Shi, J. & Schlenoff, J. B. Control of Dynamics in Polyelectrolyte Complexes by Temperature and Salt. *Macromolecules* **52**, 1930-1941 (2019). https://doi.org:10.1021/acs.macromol.8b02577

32 Tekaat, M., Butergerds, D., Schonhoff, M., Fery, A. & Cramer, C. Scaling properties of the shear modulus of polyelectrolyte complex coacervates: a time-pH superposition principle. *Phys. Chem. Chem. Phys.* **17**, 22552-22556 (2015). https://doi.org:10.1039/c5cp02940f

33 Li, L., Srivastava, S., Meng, S., Ting, J. M. & Tirrell, M. V. Effects of Non-Electrostatic Intermolecular Interactions on the Phase Behavior of pH-Sensitive Polyelectrolyte Complexes. *Macromolecules* **53**, 7835-7844 (2020). https://doi.org:10.1021/acs.macromol.0c00999

34 Spruijt, E., Westphal, A. H., Borst, J. W., Cohen Stuart, M. A. & van der Gucht, J. Binodal Compositions of Polyelectrolyte Complexes. *Macromolecules* **43**, 6476-6484 (2010). https://doi.org:10.1021/ma101031t

35 Spruijt, E., Cohen Stuart, M. A. & van der Gucht, J. Linear Viscoelasticity of Polyelectrolyte Complex Coacervates. *Macromolecules* **46**, 1633-1641 (2013). https://doi.org:10.1021/ma301730n

36 Liu, Y. *et al.* Effect of Polymer Chemistry on the Linear Viscoelasticity of Complex Coacervates. *Macromolecules* **53**, 7851-7864 (2020). https://doi.org:10.1021/acs.macromol.0c00758

37 Meng, X. *et al.* Electrospinning Fibers from Oligomeric Complex Coacervates: No Chain Entanglements Needed. *Macromolecules* **54**, 5033-5042 (2021). https://doi.org:10.1021/acs.macromol.1c00397

38 Peng, B. & Muthukumar, M. Modeling competitive substitution in a polyelectrolyte complex. *J. Chem. Phys.* **143**, 243133 (2015). https://doi.org:10.1063/1.4936256

39 Tabandeh, S. & Leon, L. Engineering Peptide-Based Polyelectrolyte Complexes with Increased Hydrophobicity. *Molecules* **24**, 868 (2019). https://doi.org:10.3390/molecules24050868

40 Tabandeh, S., Lemus, C. E. & Leon, L. Deciphering the Role of pi-Interactions in Polyelectrolyte Complexes Using Rationally Designed Peptides. *Polymers (Basel)* **13**, 2074 (2021). https://doi.org:10.3390/polym13132074

41 Vieregg, J. R. *et al.* Oligonucleotide-Peptide Complexes: Phase Control by Hybridization. *J. Am. Chem. Soc.* **140**, 1632-1638 (2018). https://doi.org:10.1021/jacs.7b03567

42 Huang, J., Morin, F. J. & Laaser, J. E. Charge-Density-Dominated Phase Behavior and Viscoelasticity of Polyelectrolyte Complex Coacervates. *Macromolecules* **52**, 4957-4967 (2019). https://doi.org:10.1021/acs.macromol.9b00036

43 Huang, J. & Laaser, J. E. Charge Density and Hydrophobicity-Dominated Regimes in the Phase Behavior of Complex Coacervates. *ACS Macro Letters* **10**, 1029-1034 (2021). https://doi.org:10.1021/acsmacrolett.1c00382

44 Rumyantsev, A. M. *et al.* Controlling Complex Coacervation via Random Polyelectrolyte Sequences. *ACS Macro Lett* **8**, 1296-1302 (2019). https://doi.org:10.1021/acsmacrolett.9b00494

45 Neitzel, A. E. *et al.* Polyelectrolyte Complex Coacervation across a Broad Range of Charge Densities. *Macromolecules* **54**, 6878-6890 (2021). https://doi.org:10.1021/acs.macromol.1c00703

46 Madinya, J. J. *et al.* Surface Charge Density and Steric Repulsion in Polyelectrolyte–Surfactant Coacervation. *Macromolecules* **56**, 3973-3988 (2023). https://doi.org:10.1021/acs.macromol.3c00464

47 Kapelner, R. A., Yeong, V. & Obermeyer, A. C. Molecular determinants of protein-based coacervates. *Curr Opin Colloid Interface Sci* **52**, 101407 (2021). https://doi.org:10.1016/j.cocis.2020.101407

48 Obermeyer, A. C., Mills, C. E., Dong, X. H., Flores, R. J. & Olsen, B. D. Complex coacervation of supercharged proteins with polyelectrolytes. *Soft Matter* **12**, 3570-3581 (2016). https://doi.org:10.1039/c6sm00002a

49 Kapelner, R. A. & Obermeyer, A. C. Ionic polypeptide tags for protein phase separation. *Chem Sci* **10**, 2700-2707 (2019). https://doi.org:10.1039/c8sc04253e

50 Cummings, C. S. & Obermeyer, A. C. Phase Separation Behavior of Supercharged Proteins and Polyelectrolytes. *Biochemistry* **57**, 314-323 (2018). https://doi.org:10.1021/acs.biochem.7b00990

51 Blocher McTigue, W. C. & Perry, S. L. Design rules for encapsulating proteins into complex coacervates. *Soft Matter* **15**, 3089-3103 (2019). https://doi.org:10.1039/c9sm00372j

52 Zhang, P., Shen, K., Alsaifi, N. M. & Wang, Z.-G. Salt Partitioning in Complex Coacervation of Symmetric Polyelectrolytes. *Macromolecules* **51**, 5586-5593 (2018). https://doi.org:10.1021/acs.macromol.8b00726

53 Qin, J. & de Pablo, J. J. Criticality and Connectivity in Macromolecular Charge Complexation. *Macromolecules* **49**, 8789-8800 (2016). https://doi.org:10.1021/acs.macromol.6b02113

54 Salehi, A. & Larson, R. G. A Molecular Thermodynamic Model of Complexation in Mixtures of Oppositely Charged Polyelectrolytes with Explicit Account of Charge Association/Dissociation. *Macromolecules* **49**, 9706-9719 (2016). https://doi.org:10.1021/acs.macromol.6b01464

55 Rubinstein, M., Liao, Q. & Panyukov, S. Structure of Liquid Coacervates formed by Oppositely Charged Polyelectrolytes. *Macromolecules* **51**, 9572-9588 (2018). https://doi.org:10.1021/acs.macromol.8b02059

56 Delaney, K. T. & Fredrickson, G. H. Polymer field-theory simulations on graphics processing units. *Comput. Phys. Commun.* **184**, 2102-2110 (2013). https://doi.org:10.1016/j.cpc.2013.04.002

57 Adhikari, S., Prabhu, V. M. & Muthukumar, M. Lower Critical Solution Temperature Behavior in Polyelectrolyte Complex Coacervates. *Macromolecules* **52**, 6998-7004 (2019). https://doi.org:10.1021/acs.macromol.9b01201

58 Ou, Z. & Muthukumar, M. Entropy and enthalpy of polyelectrolyte complexation: Langevin dynamics simulations. *J. Chem. Phys.* **124**, 154902 (2006). https://doi.org:10.1063/1.2178803

59 Heldt, C. L., Zahid, A., Vijayaragavan, K. S. & Mi, X. Experimental and computational surface hydrophobicity analysis of a non-enveloped virus and proteins. *Colloids Surf B* **153**, 77-84 (2017). https://doi.org:10.1016/j.colsurfb.2017.02.011

60 Mi, X., Bromley, E. K., Joshi, P. U., Long, F. & Heldt, C. L. Virus Isoelectric Point Determination Using Single-Particle Chemical Force Microscopy. *Langmuir* **36**, 370-378 (2020). https://doi.org:10.1021/acs.langmuir.9b03070

61 Hoffmann, K. Q. *et al.* A molecular view of the role of chirality in charge-driven polypeptide complexation. *Soft Matter* **11**, 1525-1538 (2015). https://doi.org:10.1039/c4sm02336f

62 Pacalin, N. M., Leon, L. & Tirrell, M. Directing the phase behavior of polyelectrolyte complexes using chiral patterned peptides. *The European Physical Journal Special Topics* **225**, 1805-1815 (2016). https://doi.org:10.1140/epjst/e2016-60149-6

63 Perry, S. L. *et al.* Chirality-selected phase behaviour in ionic polypeptide complexes. *Nat Commun* **6**, 6052 (2015). https://doi.org:10.1038/ncomms7052

64 Heldt, C. L. *et al.* A colorimetric assay for viral agents that produce cytopathic effects. *J. Virol. Methods* **135**, 56-65 (2006).

65 Joshi, P. U. *et al.* Osmolyte enhanced aqueous two-phase system for virus purification. *Biotechnol Bioeng* **118**, 3251-3262 (2021). https://doi.org:10.1002/bit.27849

66 Simpson, A. A. *et al.* The structure of porcine parvovirus: comparison with related viruses. *J. Mol. Biol.* **315**, 1189-1198 (2002). https://doi.org:10.1006/jmbi.2001.5319

67 Arnold, E. & Rossmann, M. G. The use of molecular-replacement phases for the refinement of the human rhinovirus 14 structure. *Acta Crystallogr Sect A: Crystallogr* **44**, 270-283 (1988).

68 Jurrus, E. *et al.* Improvements to the APBS biomolecular solvation software suite. *Protein Sci.* **27**, 112-128 (2018). https://doi.org:10.1002/pro.3280

69 Unni, S. *et al.* Web servers and services for electrostatics calculations with APBS and PDB2PQR. *J. Comput. Chem.* **32**, 1488-1491 (2011). https://doi.org:10.1002/jcc.21720

70 Pettersen, E. F. *et al.* UCSF ChimeraX: Structure visualization for researchers, educators, and developers. *Protein Sci.* **30**, 70-82 (2021). https://doi.org:10.1002/pro.3943

71 Ghose, A. K., Viswanadhan, V. N. & Wendoloski, J. J. Prediction of Hydrophobic (Lipophilic) Properties of Small Organic Molecules Using Fragmental Methods: An Analysis of ALOGP and CLOGP Methods. *J. Phys. Chem. A* **102**, 3762-3772 (1998).

72 Carrillo-Tripp, M., Montiel-Garcia, D. J., Brooks, C. L., 3rd & Reddy, V. S. CapsidMaps: protein-protein interaction pattern discovery platform for the structural analysis of virus capsids using Google Maps. *J Struct Biol* **190**, 47-55 (2015). https://doi.org:10.1016/j.jsb.2015.02.003

73 Montiel-Garcia, D. *et al.* VIPERdb v3.0: a structure-based data analytics platform for viral capsids. *Nucleic Acids Res.* **49**, D809-D816 (2021). https://doi.org:10.1093/nar/gkaa1096

74 Jacobs, S. E., Lamson, D. M., St George, K. & Walsh, T. J. Human rhinoviruses. *Clin Microbiol Rev* **26**, 135-162 (2013). https://doi.org:10.1128/CMR.00077-12

75 Arnold, E. *et al.* The structure determination of a common cold virus, human rhinovirus 14. *Acta Crystallogr. Sect. A:Crystallogr.* **43**, 346-361 (1987).

76 Smith, T. J. *et al.* The site of attachment in human rhinovirus 14 for antiviral agents that inhibit uncoating. *Science* **233**, 1286-1293 (1986).

77 Ainavarapu, S. R. *et al.* Contour length and refolding rate of a small protein controlled by engineered disulfide bonds. *Biophys J* **92**, 225-233 (2007). https://doi.org:10.1529/biophysj.106.091561

78 Langevin, D. Complexation of oppositely charged polyelectrolytes and surfactants in aqueous solutions. A review. *Adv. Colloid Interface Sci.* **147-148**, 170-177 (2009). https://doi.org:10.1016/j.cis.2008.08.013

79 Meingast, C., Joshi, P.U., Turpeinen, D.G., Xu, X., Holstein, M., Feroz, H., Ranjan, S., Ghose, S., Li, Z.J., Heldt, C.L. Physiochemical Properties of Enveloped Viruses and Arginine Dictate Inactivation. *Biotechnol J* **16**, 2000342 (2021).

80 Meingast, C. & Heldt, C. L. Arginine-enveloped virus inactivation and potential mechanisms. *Biotechnol Prog* **36**, e2931 (2020). https://doi.org:10.1002/btpr.2931

81 Tlaxca, J. L., Ellis, S. & Remmele, R. L., Jr. Live attenuated and inactivated viral vaccine formulation and nasal delivery: potential and challenges. *Adv Drug Deliv Rev* **93**, 56-78 (2015). https://doi.org:10.1016/j.addr.2014.10.002

82 Ma, C. D., Wang, C., Acevedo-Velez, C., Gellman, S. H. & Abbott, N. L. Modulation of hydrophobic interactions by proximally immobilized ions. *Nature* **517**, 347-350 (2015). https://doi.org:10.1038/nature14018

83 Areo, O., Joshi, P. U., Obrenovich, M., Tayahi, M. & Heldt, C. L. Single-Particle Characterization of SARS-CoV-2 Isoelectric Point and Comparison to Variants of Interest. *Microorganisms* **9**, 1606 (2021). https://doi.org:10.3390/microorganisms9081606

84 Eisenberg, D., Schwarz, E., Komaromy, M. & Wall, R. Analysis of membrane and surface protein sequences with the hydrophobic moment plot. *J. Mol. Biol.* **179**, 125-142 (1984).

85 Banani, S. F., Lee, H. O., Hyman, A. A. & Rosen, M. K. Biomolecular condensates: organizers of cellular biochemistry. *Nat Rev Mol Cell Biol* **18**, 285-298 (2017). https://doi.org:10.1038/nrm.2017.7

86 Berry, J., Brangwynne, C. P. & Haataja, M. Physical principles of intracellular organization via active and passive phase transitions. *Rep. Prog. Phys.* **81**, 046601 (2018). https://doi.org:10.1088/1361-6633/aaa61e

87 Fossat, M. J., Zeng, X. & Pappu, R. V. Uncovering Differences in Hydration Free Energies and Structures for Model Compound Mimics of Charged Side Chains of Amino Acids. *J. Phys. Chem. B* **125**, 4148-4161 (2021). https://doi.org:10.1021/acs.jpcb.1c01073

88 Harmon, T. S., Holehouse, A. S. & Pappu, R. V. Differential solvation of intrinsically disordered linkers drives the formation of spatially organized droplets in ternary systems of linear multivalent proteins. *New J Phys* **20**, 045002 (2018). https://doi.org:10.1088/1367-2630/aab8d9

89 Pak, C. W. *et al.* Sequence Determinants of Intracellular Phase Separation by Complex Coacervation of a Disordered Protein. *Mol Cell* **63**, 72-85 (2016). https://doi.org:10.1016/j.molcel.2016.05.042

90 Ruff, K. M. *et al.* Sequence grammar underlying the unfolding and phase separation of globular proteins. *Molecular Cell* **82**, 3193-3208.e3198 (2022). https://doi.org:10.1016/j.molcel.2022.06.024

91 Etibor, T. A., Yamauchi, Y. & Amorim, M. J. Liquid Biomolecular Condensates and Viral Lifecycles: Review and Perspectives. *Viruses* **13**, 366 (2021). https://doi.org:10.3390/v13030366

92 Charman, M. *et al.* A viral biomolecular condensate coordinates assembly of progeny particles. *Nature* **616**, 332-338 (2023). https://doi.org:10.1038/s41586-023-05887-y

93 Dubin, P. L., Gao, J. & Mattison, K. Protein Purification by Selective Phase Separation with Polyelectrolytes. *Sep. Purif. Methods* **23**, 1-16 (2006). https://doi.org:10.1080/03602549408001288

94 Wang, Y.-f., Gao, J. Y. & Dubin, P. L. Protein Separation via Polyelectrolyte Coacervation: Selectivity and Efficiency. *Biotechnol. Progr.* **12**, 356-362 (1996). https://doi.org:https://doi.org/10.1021/bp960013+

95 Xu, Y., Mazzawi, M., Chen, K., Sun, L. & Dubin, P. L. Protein purification by polyelectrolyte coacervation: influence of protein charge anisotropy on selectivity. *Biomacromolecules* **12**, 1512-1522 (2011). https://doi.org:10.1021/bm101465y

96 Zhou, J. *et al.* Protein separation by sequential selective complex coacervation. *J. Colloid Interface Sci.* **650**, 2065-2074 (2023). https://doi.org:10.1016/j.jcis.2023.06.119

97 Kawamura, A., Harada, A., Kono, K. & Kataoka, K. Self-assembled nano-bioreactor from block ionomers with elevated and stabilized enzymatic function. *Bioconjug Chem* **18**, 1555-1559 (2007). https://doi.org:10.1021/bc070029t

98 Martin, N. *et al.* Prevention of thermally induced aggregation of IgG antibodies by noncovalent interaction with poly(acrylate) derivatives. *Biomacromolecules* **15**, 2952-2962 (2014). https://doi.org:10.1021/bm5005756

99 Zhao, M. & Zacharia, N. S. Protein encapsulation via polyelectrolyte complex coacervation: Protection against protein denaturation. *J. Chem. Phys.* **149**, 163326 (2018). https://doi.org:10.1063/1.5040346